THE JOURNAL OF PHYSICAL CHEMISTRY A
A JOURNAL OF THE AMERICAN CHEMICAL SOCIETY

pubs.acs.org/JPCA Article

Investigation of Freezing-Induced Anionic Interplay in Acoustically Levitated Artificial Seawater Droplets

Frank Liang, Souvick Biswas, Nils W. Melbourne, Koushik Mondal, Rui Sun, and Ralf Kaiser*

Cite This: *J. Phys. Chem. A* 2026, 130, 229−241 Read Online

ACCESS | Metrics & More | Article Recommendations | Supporting Information

ABSTRACT: Freezing of aqueous droplets plays a pivotal role in atmospheric processes, which is often governed by the soluble earth-abundant salts, minerals and their corresponding ions. These droplet freezing events in turn control the physical state, reactivity, and lifetime of aerosols at subzero temperature in the Celsius scale. In this study, we investigated the freezing behavior of artificial seawater droplets containing chloride and polyatomic anions like sulfate and bicarbonate using a cryogenically cooled acoustic levitation setup coupled with in situ Raman spectroscopy, enabling contact-free measurements of evolving ionic speciation. Spectral comparisons reveal that sulfate undergoes symmetry lowering and associated spectral broadening upon freezing, while bicarbonate remains a spectator at the given below-detection limit concentration. Complementary density functional theory calculations provide independent evidence of sulfate's symmetry lowering upon freezing and the associated Raman-band broadening. Control freezing experiments with pure sulfate, bicarbonate and their mixture further demonstrate that sulfate is the pivotal component which solely initiates a distinct ionic transformation during ice formation, providing molecular-level insight into the structural evolution of seawater ice crystals. This study directs the possibility of emerging heterogeneous interactions between sulfate-rich ice surfaces and atmospheric gases, including pollutants and refrigerants, underscoring their potential role in multiphase atmospheric chemistry.

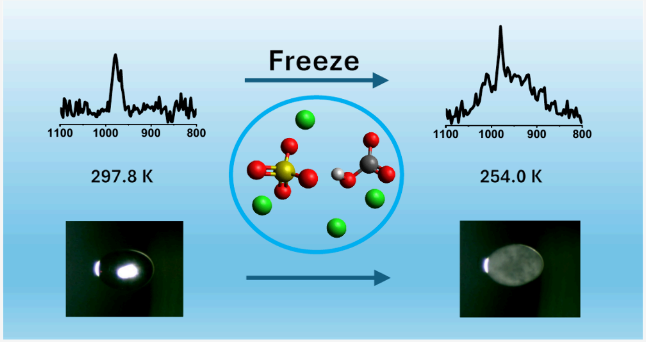

1. INTRODUCTION

Approximately 71% of Earth's surface is covered by seawater, which constitutes 97% of total water content of planet Earth among which additional 3% frozen in glaciers and ice caps.[1] The major dissolved constituents of seawater are chloride (Cl^-), sodium (Na^+), sulfate (SO_4^{2-}), magnesium (Mg^{2+}), calcium (Ca^{2+}), potassium (K^+), and, to a lesser concentration, bicarbonate ions (HCO_3^-).[2,3] While the relative proportions of these ions remain broadly consistent due to the principle of constant proportions, regional variations can occur in response to factors such as biogeochemical cycling, riverine input, hydrothermal activity, and dynamic exchanges between the ocean and atmosphere.[4] For instance, the magnesium to calcium ratio can vary with geographic location and water mass origin. On average, the total salinity of seawater is approximately 3.5% by weight.[2,3]

In polar oceans, seawater freezing represents a common and climatically significant process. Modern ocean salinity depresses the freezing point of seawater by approximately 2 K, and the presence of dissolved salts strongly influences ice crystal structure, growth rates, and brine channel formation.[5,6] Dissolved ions interfere with the formation of the ordered hydrogen-bond network required for ice nucleation by disrupting O−H bonding between water molecules. This disruption requires a lower temperature for water molecules to arrange into the crystalline ice lattice, effectively lowering the freezing point relative to pure water.[7,8] Ion-specific effects have also been reported. For example, fluoride (F^-) and ammonium (NH_4^+) ions can alter both the morphology and growth rate of ice crystals in electrolyte solutions.[9] In biological systems, ions in the surrounding medium can modify the efficiency of bacterial ice nucleators via interactions with nucleating proteins at the cell surface.[10] During freezing, salts are largely excluded from the ice lattice, resulting in brine rejection and the formation of highly saline inclusions or surface brine layers. This process alters the physical properties of sea ice compared to pure ice and plays a key role in ocean-atmosphere exchanges. Seasonal and perennial sea ice formation in the Arctic not only impacts salinity and stratification but also modulates regional climate through albedo changes and heat fluxes.[11,12] Although the overall volume, extent, and age of Arctic Sea ice are declining, recent evidence suggests that

Received: September 5, 2025
Revised: November 25, 2025
Accepted: November 26, 2025
Published: December 16, 2025

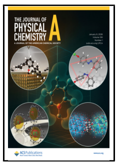

https://doi.org/10.1021/acs.jpca.5c06239

winter sea ice production has increased in some regions despite pronounced wintertime Arctic warming.[13]

Among the dominant ions in seawater, sulfate plays a particularly important role. It is the dominant oxidized form of sulfur in oxygenated seawater and a central component of the marine sulfur cycle. Microbial sulfate reduction produces hydrogen sulfide, which can subsequently be reoxidized to sulfate by sulfur-oxidizing microorganisms, establishing a dynamic biogeochemical loop.[14,15] Beyond its microbial cycling, sulfate contributes to aerosol formation, cloud condensation nuclei activity, and heterogeneous chemistry relevant to climate processes. Bicarbonate (HCO_3^-) is similarly fundamental to marine chemistry. As the most abundant dissolved inorganic carbon species, it underpins the ocean's role as a major sink for atmospheric carbon dioxide (CO_2).[16] Bicarbonate, together with carbonate (CO_3^{2-}), provides much of the ocean's buffering capacity, thereby moderating the effects of anthropogenic CO_2 uptake on seawater pH and ocean acidification.[16] In addition, many marine photosynthetic organisms utilize bicarbonate directly as a carbon source, linking it to primary productivity and carbon cycling.[17]

Sea spray aerosols (SSAs) are the most abundant type of marine aerosol. They consist primarily of the same salts and ions found in seawater such as sodium chloride (NaCl), with smaller amounts of magnesium, calcium, sulfate, and potassium ions. They are generated when wind-driven waves produce bubbles that burst at the ocean surface, ejecting saline droplets into the atmosphere.[18,19] These droplets can remain airborne as aerosols, influencing cloud microphysics and radiative forcing. Observations in coastal regions such as Hawaii reveal significantly higher concentrations of giant sea salt aerosols compared to those over the open ocean, with these supermicron particles playing an important role in local cloud formation and precipitation processes.[18,19] SSAs can act as efficient ice-nucleating particles (INPs), promoting ice crystal formation at higher temperatures than homogeneous freezing would allow.[20,21] This ability can influence mixed-phase cloud properties, cloud lifetime, precipitation onset, and radiative balance. Their impacts include enhancing snow and ice precipitation, modifying regional hydrological cycles, and introducing uncertainties into climate model predictions due to limited representation of SSA-INP activity and its dependence on seawater composition.[22−25] Given their high surface-to-volume ratio and heterogeneous composition, SSAs share physicochemical similarities with the saline droplets examined in this study, making them an important atmospheric analog for interpreting our results.

Because the behavior of sea spray and mixed aerosols reflects the underlying chemistry of freezing seawater, it is important to first consider what is already known about how salts reorganize during the liquid-to-ice transition. While the effects of freezing on bulk seawater salinity and ice morphology have been extensively studied, fewer investigations have examined the molecular-scale chemical changes induced by freezing, particularly in relation to salt-specific chemistry. Prior work has documented desalination effects during freezing and ion-specific migration or segregation behaviors in freezing saline systems.[26−28] Recent surface-specific measurements on artificial seawater also show that realistic oceanic ion mixtures, together with trace surfactants, substantially reorganize interfacial composition and reactivity, altering the surface propensity of sulfate, magnesium, and other ions and thereby affecting heterogeneous chemistry at the air−water boundary.[29] Using liquid-jet photoelectron spectroscopy and surface-tension measurements on artificial seawater containing the major seawater ions at realistic concentrations, it has been shown that even a nominal 0.12 fraction of a monolayer of charged surfactant can substantially remodel interfacial ion populations. In particular, interfacial sulfate can be modulated by about an order of magnitude depending on surfactant charge, with trends governed by electrostatic attraction or repulsion and further tuned by ionic strength and specific interactions with Mg^{2+} and Ca^{2+}. The liquid-jet photoelectron spectroscopy approach probes only the top few nanometers, directly reporting interfacial composition in these mixed ion-surfactant systems.[29] In addition, electrical potentials can develop during droplet freezing due to ion partitioning. The classic Workman-Reynolds freezing potential (WRFP) appears during slow front propagation at small supercoolings and can reach large voltages; at higher supercoolings a distinct, faster "alternating-spike" potential accompanies the dendritic stage and can set the polarity and magnitude of the subsequent WRFP-like signal. The dendritic-stage amplitude scales with ΔT and depends on ion concentration, with a breakdown concentration in the 10^{-4}−10^{-2} mol/L range.[30]

However, there remains a gap in literature in understanding how molecular and ionic interactions govern the evolving structure and chemistry of seawater during freezing, especially through approaches that can capture changes occurring in both the bulk and interfacial regions. Addressing this knowledge gap in the underlying chemistry specifically at the atmospherically relevant droplet level is the primary motivation of the present work.

Another potential process of atmospheric relevance is the interaction between these seawater-derived salts and anthropogenic halogenated refrigerants. While often considered relatively inert, chlorofluorocarbons such as trichlorofluoromethane (CCl_3F) and dichlorodifluoromethane (CCl_2F_2) have been detected both in the marine atmosphere and within the ocean water column of regions such as the Greenland and Norwegian Seas.[31] These compounds have historically been used as tracers for ocean circulation studies due to their measurable solubility and persistence,[31−35] indicating their capacity for gas−aqueous phase transfer. Although the detailed mechanisms of uptake and subsequent interfacial reactivity remain uncertain, the presence of salts such as sulfate in seawater or sea spray aerosols suggests the possibility of unique ionic equilibria and heterogeneous interactions with refrigerants upon freezing, with implications for both atmospheric chemistry and pollutant transformation.

An understanding of these processes requires first an in-depth spectroscopic characterization of single droplets of seawater proxies. To achieve this, we employed a surface-free droplet levitation approach in an acoustic trap combined with Raman spectroscopy to monitor the freezing of artificial seawater and model salt solutions.[36,37] The levitated droplet geometry eliminates container wall effects and, with its high surface-to-volume ratio, enhances the role of interfacial chemistry compared to bulk-phase systems. Acoustic levitation has been used to study freezing of neat and salty droplets with synchronized high-speed IR/VIS imaging, providing time-resolved temperature fields and interior morphology during supercooling and recalescence; related setups also integrate high-speed cameras and can be operated with an acoustic levitator in a controlled cooling chamber.[30,38] This experimental configuration more closely represents the physicochemical environment of atmospheric aerosols, enabling direct observation of freezing-induced ionic and structural transformations under atmospherically relevant conditions. In this work, we explore the behavior of sulfate and bicarbonate ions during the freezing of seawater analogues, and show how their spectroscopic signatures reflect distinct solvation environments and protonation pathways. These results provide new molecular-level insight into the evolution of ice structure in saline systems and reveal an unexpectedly complex anionic chemistry that emerges upon freezing.

2. EXPERIMENTAL SECTION

2.1. Artificial Seawater and Salt Solution Preparation. Artificial seawater (ASW) was prepared following the recipe detailed in Foltz et al.[39] The resulting seawater solution corresponds to 3.5% salinity by weight. In 53.70 g of distilled water, the following salts were added: 1.52 g of sodium chloride (NaCl, Fisher Chemical, ≥99.0% purity), 0.194 g of magnesium sulfate ($MgSO_4$, Fisher Chemical, ≥99.0% purity), 0.295 g of magnesium chloride hexahydrate ($MgCl_2 \cdot 6H_2O$, Sigma-Aldrich, ≥99.995% purity), 0.06 g of calcium chloride dihydrate ($CaCl_2 \cdot 2H_2O$, Fisher Chemical, ≥99.0 purity), 0.0414 g of potassium chloride (KCl, Sigma-Aldrich, ≥99.0% purity), and 0.0170 g of sodium bicarbonate ($NaHCO_3$, Fisher Chemical, ≥99.7 purity). In addition, 0.838 g of $MgSO_4$ was added to 23.9 g of distilled water for the desired sulfate solution (3.5% w/w). Similarly, bicarbonate solution was prepared by adding 0.884 g of $NaHCO_3$ to 25.3 g of distilled water.

2.2. Surface-Free Levitator Setup in a Cryogenically Cooled Process Chamber. In the acoustic levitator apparatus utilized in this experiment (Figure 1),[37] ultrasonic sound waves at a frequency of 58 kHz are generated by a piezoelectric transducer and reflected off a concave plate positioned vertically upward, thereby creating a standing wave. These sound waves generate acoustic radiation pressure, enabling a liquid droplet or a small solid particle to levitate just below one of the pressure minima of the standing wave. The distance between the transducer and reflector is calibrated to 2.5 times the wavelength of the sound wave (approximately 14.8 mm), resulting in a total of five pressure nodes. However, only the second and third pressure nodes above the ultrasonic transducer are suitable for levitation. The maximum diameter of droplets or particles that can be stably levitated in this apparatus is around 3 mm, while the minimum size can be as small as 15 μm. To capture visuals of the freezing process, the chamber is also equipped with a Phantom Miro 3a10 camera that was aligned with the levitated sample via an optical viewport. The camera operates at a repetition rate of up to 1 kHz. The levitator assembly is housed within a pressure-compatible process chamber, approximately 15 L in volume, constructed from low-carbon stainless steel 304. This design allows for levitation in either inert or highly reactive gases to facilitate the investigation of chemical reactions. The process chamber is equipped with spectroscopic tools (Raman) along with the visualization equipment to monitor any significant chemical or physical changes in the levitated samples.[37,40,41]

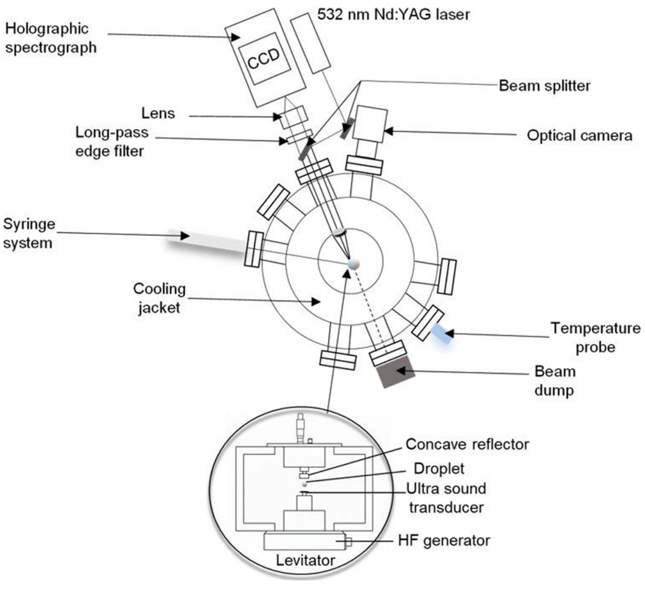

Figure 1. Schematic top view of the complete levitator apparatus displaying the ultrasonic levitator, process chamber, Nd:YAG laser, Raman spectrometer, temperature probe, cooling jacket containing liquid nitrogen, and optical camera. A photograph of the levitator setup is depicted in Figure S1 of the Supporting Information (SI).

A custom cylindrical cooling jacket, filled with liquid nitrogen, is inserted from the top, and positioned between the chamber wall and the levitator unit to cool the internal environment.[36] The cooling jacket features customized cuts to accommodate all spectroscopic and camera probes and is connected to a liquid nitrogen dewar located externally. Additionally, the process chamber is well insulated to enhance the cooling efficiency. The internal gas temperature is monitored by a silicon diode sensor, which provides an accurate reading of the chamber atmosphere. During the droplet freezing processes, the droplet was allowed to remain in the acoustic trap for 30 min without observing any spectral changes. This is to confirm that the droplet temperature was equilibrated with the chamber environment temperature as measured through the silicon diode temperature sensor. During all experiments, the chamber was filled with nitrogen gas (Matheson, Research Purity 99.9999%) at a temperature of 293 K and a total pressure of 760 Torr.

2.3. Raman Spectroscopy. In the Raman spectrometer, vibrational transitions are excited by a 532 nm line from a diode-pumped, Q-switched Nd:YAG laser (CrystaLaser, model QL532-1W0), which has a beam diameter of 0.35 mm and a divergence angle of 3.8 mR. The laser outputs an average power of approximately 200 mW with a pulse width of 13.5 ns, operating at a repetition rate of 1 kHz. The laser beam is introduced into the chamber through an antireflection-coated window, followed by a mirror (Edmund Optics, model NT45-991, >99% reflectance) and a dichroic beam splitter (Semrock, RazorEdge, model LPD01-532RU- 25 × 36 × 2.0). A plano-convex lens with a focal length of 60 mm focuses the laser beam onto the sample, creating a spot with a diameter (1/e2) of approximately 20 μm. The Raman-shifted photons, backscattered from the droplet, pass through an ultrasteep long-pass edge filter (Semrock, model LP03-532RE-25) to eliminate elastically scattered 532 nm laser light. The resultant backscattered photons are then focused by a 50 mm f/1.8 camera lens (Nikon, Nikkor 2137) into a HoloSpec f/1.8 holographic imaging spectrograph (Kaiser Optical Systems, model 2004500-501 and Holoplex HPG-532) equipped with a PI-Max 2 Intensified Charge-Coupled Device (ICCD) camera (Princeton Instruments) through a 100 μm slit. The CCD

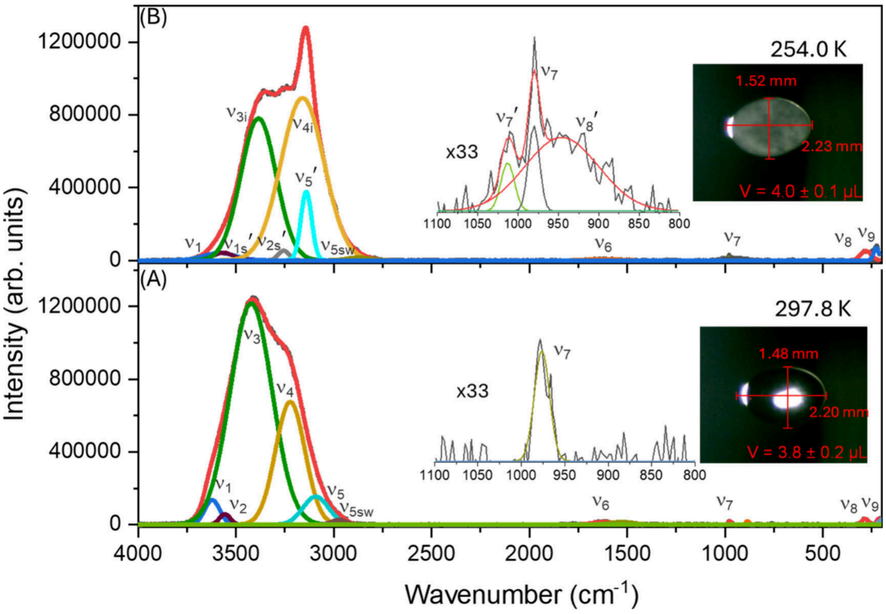

Figure 2. Deconvoluted Raman spectra of ASW (aqueous solution of 3.5% salinity by weight) in (A) liquid state at 297.8 K and (B) frozen solid state, equilibrated with the surrounding gaseous environment at 254.0 K, as determined by the silicon diode sensor. Zoomed-in spectra at the 800–1100 cm^{-1} region where the sulfate stretching peak occurs is shown in both states respectively, depicting drastic changes upon freezing. Detailed peak assignments can be found in Tables 1 and 2. Also shown are the images captured by the high-speed optical camera along with measurement of the droplet size. Droplet size was determined through pixel measurements from captures of the optical camera, error bars originate from the measurement uncertainty. The droplet undergoes nominal volume increase (~5%) upon freezing, otherwise remained consistent during the freezing process, as well as across all experiments with various droplet compositions.

detector consists of 1024 × 256 pixels, each with a spatial resolution of 26 μm. Spectra are collected over Raman-shift ranges of 200–2450 cm^{-1} and 2400–4000 cm^{-1} simultaneously, achieved by dispersing the total signal using two overlaid holographic transmission gratings. The resolution of the Raman spectrometer is 9 cm^{-1}. Both the excitation laser and the detector operate at a 1 kHz repetition rate, synchronized via a pulse generator, Quantum Composer Plus, model-9518. To isolate the Raman scattering signal, the pulse width for the ICCD detector is typically set around 50 ns, with accumulation times for each spectral trace ranging from 5 to 100 s. For the experiments presented, a typical gate delay of 480–500 ns was employed, with gates per exposure fixed at 1000 shots. This is the optimal gate delay to suppress any fluorescence background, which evolves at a longer delay than Raman scattering. The Raman spectrometer was calibrated by recording Raman spectra for levitating droplets of cyclohexane (C_6H_{12}), toluene ($C_6H_5CH_3$), and acetonitrile (CH_3CN).[37,40]

2.4. Computational Methods. Geometry optimizations and vibrational frequency calculations were performed for sulfate (SO_4^{2-}), carbonate (CO_3^{2-}), and bicarbonate (HCO_3^-) encapsulated in an ice I_h cluster containing 42 water molecules. All atoms were allowed to relax during geometry optimization. Additional optimization and frequency calculations were performed for the isolated (di)anions with the solvation model density (SMD) continuum water solvation model applied to simulate the experimental seawater environment.[42] All geometry optimizations and vibrational frequency calculations were performed with the NWChem program.[43] Given the size of the structures studied, the use of highly correlated methods and large basis sets was not practical. Calculations were performed using B3LYP-D3 density functional theory with the 6-31+G* basis set. The D3 dispersion correction was necessary for accurately modeling hydrogen bonding interactions.[44] The basis set was chosen for its inclusion of diffuse functions, which are known to be critical for describing the anionic systems. Anharmonic effects were corrected for by use of a scaling factor of 0.962 as recommended by CCCPDB.[45] Vibrational modes were visualized and labeled manually in Avogadro 2.[46] Figures were rendered using VMD.[47]

3. RESULTS AND DISCUSSION

3.1. Room Temperature Raman Spectra of Artificial Seawater (ASW) Droplets. While the levitated droplets studied here have diameters on the order of 1–2 mm (Figure 2), atmospheric sea spray aerosols span roughly 0.1–10 μm in diameter, encompassing submicron organic-enriched film drops and larger jet drops formed from bubble bursting.[18,19,21,24] The laboratory droplets thus represent bulk aqueous analogs rather than true aerosol-scale particles, though both share a high surface-to-volume ratio relative to macroscopic water volumes. Somewhat larger droplets in our case allow spectroscopic probing at single droplet level to trace molecular reorganization during freezing. Under ambient conditions (297.8 K), the Raman spectra (Figure 2A) of ASW exhibit the characteristic peak of symmetric stretching mode (ν_7) of the sulfate ion (SO_4^{2-}) centered at 981 cm^{-1}. This feature is not observed in the spectrum of pure water droplets, as shown in Figure S2 and Tables S1 and S2. This feature is widely documented in the literature and serves as a unique spectral signature of sulfate in aqueous environments.[48,49] In addition to the sulfate feature, several other Raman bands associated with water, along with feature arising from salt species present in the ASW were observed. In the room temperature spectra of aqueous droplets, signals attributable to both free or weakly hydrogen-bonded O–H

Table 1. Peak Assignments for the Deconvoluted Raman Spectrum of ASW (3.5% Salinity by Weight) Droplets at 297.8 K[a]

Peak	Experimental wavenumber (cm^{-1})	Carrier	Peak assignment	Literature wavenumber (cm^{-1})	Reference
ν_1	3622	H_2O (surface)	Free or weakly bond O−H group (surface/interface)	3632	50, 51
ν_2	3557	H_2O (bulk)	Weakly H-bonded hydration water	∼3530	50, 52, 53
ν_3	3425	H_2O (bulk)	Bulk water O−H intermediate stretch	3435	52, 54
ν_4	3223	H_2O (deformed)	O−H stretch of deformed tetrahedral H-bond	3140 to ∼3200	50, 53, 64, 65
ν_5	3095	H_2O (bulk)	O−H stretch of ideal tetrahedral H-bond	3075	53
ν_{5sw}	2974	H_2O (bulk)	Intense O−H stretching	∼2800−3000	66, 67
ν_6	1623	H_2O	OH bend	∼1600	68, 69
ν_7	980	SO_4^{2-} (aq)	Symmetric S−O stretch in sulfate	981	48
ν_8	286	H_2O (bulk)	Translational lattice mode	∼280	36, 65
ν_9	216	H_2O (bulk)	Translational lattice mode	∼220	36, 65

[a] sw = seawater solution being the first time this mode appears.

Table 2. Peak Assignments for the Deconvoluted Raman Spectrum of Ice Crystal from Artificial Seawater Droplets (3.5% Salinity by Weight) at 254.0 K[a]

Peak	Experimental wavenumber (cm^{-1})	Carrier	Peak assignment	Literature wavenumber (cm^{-1})	Reference
ν_1	3583	H_2O (surface)	Free or weakly bond O−H group (surface/interface)	∼3530−3632	50−53
ν_{1s}'	3566	H_2O (surface)	O−H stretch of fully coordinated interfacial water molecules	∼3530	52
ν_{3i}	3380	H_2O (s)	Bulk water O−H stretch (red-shifted intermediate H-bond)	3314−3435	50, 52, 54, 57, 64, 70
ν_{2s}'	3256	H_2O (deformed)	O−H stretch of hexagonal crystal structure	∼3208	57
ν_{4i}	3160	H_2O (s)	O−H stretch in fully slightly distorted DDAA* ice	3140 to ∼3200	50, 53, 64, 65
ν_5'	3140	H_2O (s)	O−H stretch in DDAA ice	3140−3150	50, 64, 65
ν_{5sw}	2874	H_2O (bulk)	Intense O−H stretching	∼2800−3000	66, 67
ν_6	1650	H_2O (bulk)	OH bend	∼1600	68, 69
ν_7'	1013	SO_4^{2-} (aq/s)	Symmetric S−O stretch of sulfate in reduced symmetry environments	1000	71
ν_7	981	SO_4^{2-} (aq)	Symmetric S−O stretch in sulfate	981	48
ν_8'	951	SO_4^{2-} (aq/s)	Symmetric S−O stretch of sulfate in reduced symmetry environments		62, 63, 72
ν_8	280	H_2O (s)	Translational lattice mode	∼280	36, 65
ν_9	227	H_2O (s)	Translational lattice mode	∼220	36, 65

[a] * = Double donor double acceptor. i = red-shifted.

groups appear in the stretching regions as ν_1 (3622 cm^{-1}) and ν_2 (3557 cm^{-1}), respectively (Table 1). The ν_1 peak at 3622 cm^{-1} closely matches literature-reported value near 3632 cm^{-1} for weak or non-hydrogen bonded O−H stretches.[50−53] The ν_2 band appears at 3557 cm^{-1}, consistent with previous reports of similar modes at approximately 3537 cm^{-1} resembling to fully coordinated water molecules.[50] The broad peak at 3425 cm^{-1} (ν_3) corresponds to bulk water O−H stretching vibrations, while the feature near 3223 cm^{-1} (ν_4) arises from tetrahedrally coordinated water molecules slightly distorted from ideal tetrahedral geometry.[50,52−54] The ratio of intensities of these two peaks is inherently temperature-dependent and has been widely used as a semiquantitative structural indicator or "spectroscopic thermometer".[55,56] Under room temperature conditions, the ν_3 band dominates over ν_4 in spectral intensity. No detectable spectral features of bicarbonate anion are observed as the concentration is too low (0.03%).

3.2. Raman Spectra of Frozen ASW Ice. Notably, upon freezing, alteration in the spectral pattern for the broad O−H stretch region (3800−2800 cm^{-1}) is observed accompanied by spectral shifts and emergence of new bands (Figure 2B, Table 2). In particular, the ν_4 band is red-shifted to 3135 cm^{-1} (ν_{4i}) and becomes more prominent than ν_3, which also saw redshifting from 3425 cm^{-1} to 3380 cm^{-1}, on the contrary as observed in the liquid phase. Among the new bands, ν_{1s}' at 3566 cm^{-1} is assigned to the symmetric stretch of O−H in fully coordinated interfacial water.[52] The ν_{2s}' band at 3256 cm^{-1} aligns more closely to O−H stretching in hexagonally oriented crystal water structures, while the ν_5' feature at 3140 cm^{-1} corresponds to the DDAA (double donor double acceptor) O−H stretch mode.[50,57]

It is also apparent that, besides both experiencing a redshift, bands ν_3 and ν_4 undergo a change in relative bandwidth, which is shown in Tables S9 and S13. Namely, in liquid ASW, the full width at half-maximum (fwhm) of ν_3 is notably larger than ν_4 (252 cm^{-1} versus 177 cm^{-1}), whereas in the frozen crystal this trend is reversed (212 cm^{-1} versus 259 cm^{-1}). This is a reflection of the phase transition to a rigid tetrahedral lattice in which all OH groups experience nearly identical hydrogen-bonding environments, reducing inhomogeneous broadening, solvation dynamics, and producing a strongly coupled, coherent vibration.[55,56,58−61] Because these changes evolve continuously during cooling, we additionally monitored the time-dependent behavior of the O−H stretch envelope together with the sulfate ν_1 band to track the progression of the freezing event and the accompanying changes in ionic

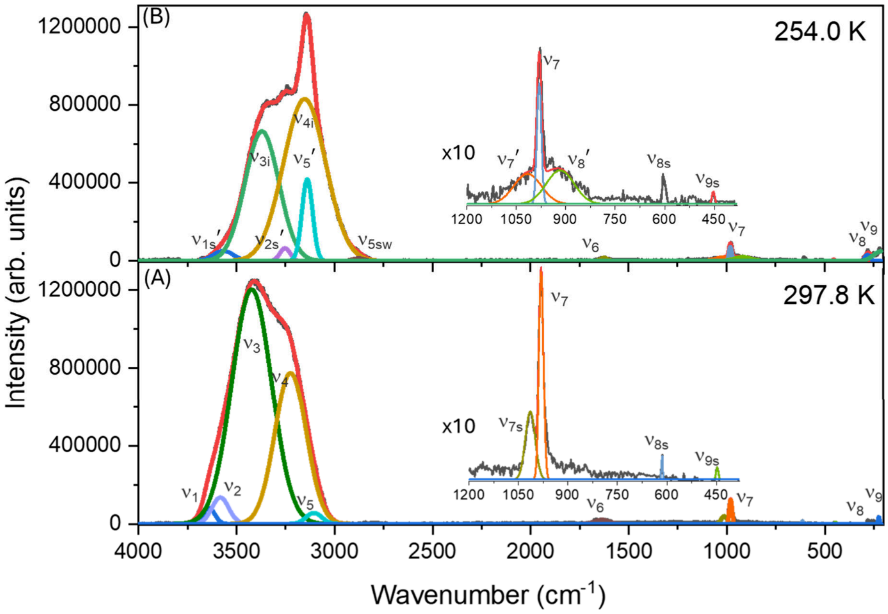

Figure 3. Deconvoluted Raman spectra of a 3.5 wt % aqueous magnesium sulfate ($MgSO_4$) solution in (A) the liquid phase at 297.8 K and (B) the frozen state equilibrated with the gaseous environment at 254.0 K, as determined by the silicon diode sensor. The spectral region from 1100 to 800 cm^{-1}, corresponding to the sulfate vibrational modes, is highlighted, revealing notable spectral broadening and intensity reduction after freezing. Peak deconvolution and assignments are summarized in Tables S3 and S4.

environments. These temporal Raman spectral traces and the corresponding kinetic profiles are provided in Figures S3 and S4. Their inclusion illustrates that freezing proceeds through an initial liquid stage, an onset of salt-induced heterogeneous nucleation, and subsequent partial and complete freezing, which together establish the context for the sulfate symmetry-lowering behavior discussed below.

The 981 cm^{-1} peak corresponding to solvated sulfate anion undergoes significant broadening upon crystallization of the droplet and indicates a decrease in integrated area upon spectral deconvolution (Figure 2B); this phenomenon is suggestive of structural perturbations in the ionic solvation environment. Two additional peaks adjacent to the primary sulfate peak (981 cm^{-1}) can be located: a low-frequency shoulder at 951 cm^{-1} and a higher-frequency weak feature in the 1013−1031 cm^{-1} range, as shown in Figure 2B. The 951 cm^{-1} component is attributed to sulfate anions occupying reduced-symmetry environments within the ice matrix. This assignment is consistent with previous findings and cannot be fit with other known species in ASW exhibiting Raman activity in this region.[62,63]

Mechanical stress or crystalline constraints can cause elongation in chemical bonds, thereby the observed red-shift in the vibrational frequency can be linked to a phenomenon applicable to the freezing-induced changes.[62] Additionally, it has been demonstrated that Raman-active modes of sulfate, including ν_2 and ν_4, can undergo splitting under symmetry-lowering conditions.[72] For example, in the case of creedite ($Ca_3Al_2SO_4(F,OH)\cdot 2H_2O$), the local symmetry reduction from T_d to C_{2v} occurs due to bidentate coordination between the sulfate ion and water molecules hydrogen-bonded to Al^{3+} centers, resulting in the splitting of the ν_2, ν_3, and ν_4 modes. Furthermore, it has been reported that in potassium sulfate (K_2SO_4) crystals, the ν_1 symmetric stretching mode can appear as low as 930.3 cm^{-1}, reinforcing the notion that deviation from ideal tetrahedral symmetry leads to spectral shifts and additional bands.[63]

The high-frequency feature at ∼1014 cm^{-1} likely arises from one of two plausible mechanisms. First, it may result from additional symmetry lowering of the sulfate tetrahedron due to the freezing-induced restructuring of the local solvation shell. This is supported by the observation of a shift of the sulfate ν_1 band from 981 to 1000 cm^{-1} when sulfate was incorporated into the apatite lattice (SSrApOH), leading to significant distortion of the tetrahedral geometry within the crystalline matrix.[71] Alternatively, this band may correspond to the bisulfate ion (HSO_4^-), which is known to exhibit Raman activity near this region.[49,73] While bisulfate formation is chemically plausible under acidic conditions, its presence in ASW is uncertain due to the relatively low concentration of bicarbonate (a potential proton donor). As detailed in the Experimental Section, the concentration of sulfate in ASW is more than 10-fold higher than that of bicarbonate (0.194 g vs 0.017 g), making significant bisulfate formation unlikely under these conditions. It is noteworthy that when sodium and sulfate ions are present in high concentrations, freezing, particularly in aerosolized particles, can promote the crystallization of sodium sulfate in the solid phase III form, especially under slightly acidic conditions.[73] A key spectral distinction between sulfate in phase III Na_2SO_4 and aqueous sulfate is the position of the ν_1 symmetric stretching band. In phase III, the band is shifted to approximately 992−996 cm^{-1}.[73] In the present study, while the dominant sulfate ν_1 band in frozen ASW remains centered at ∼981 cm^{-1}, indicating that the majority of sulfate species remain as ions within the ice matrix, a minor shift due to phase III Na_2SO_4 formation may have also contributed to this broader peak at 1013 cm^{-1}.

3.3. Plausible Dynamic Anionic Interplay during Freezing.

To further evaluate the origins of the shoulder peaks observed in ASW ice crystal, three additional solutions involving the polyatomic anions were prepared and analyzed: a pure magnesium sulfate solution, a pure sodium bicarbonate solution, and a 1:1 by-weight mixture of sulfate and

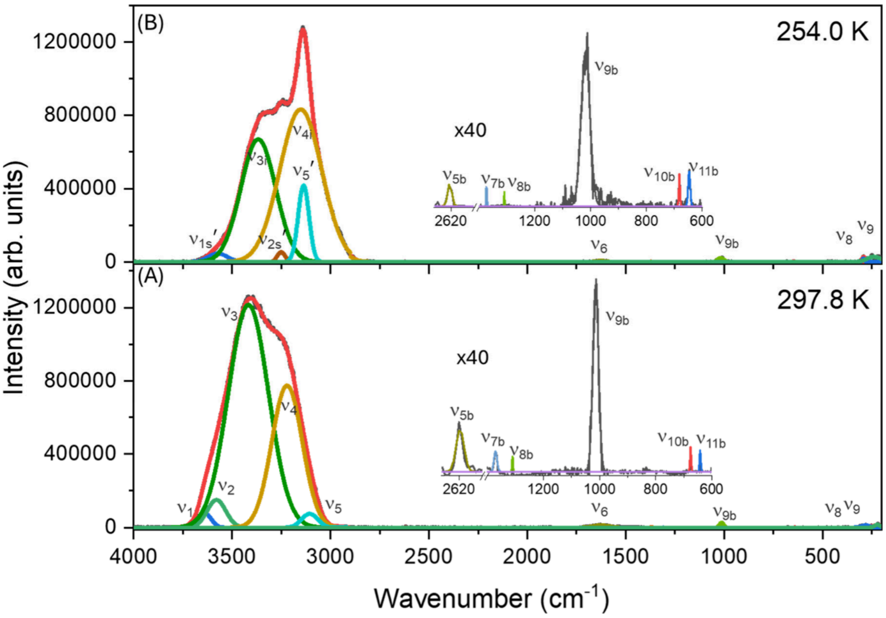

Figure 4. Comparison of deconvoluted Raman spectra for 3.5% by weight sodium bicarbonate ($NaHCO_3$) aqueous solution at (A) room temperature liquid state (297.8 K) and (B) frozen conditions (equilibrated with the surrounding gaseous environment at 254.0 K). In the 1100–800 cm^{-1} spectral segment, characteristic solvated bicarbonate-related vibrations are magnified. Refer to Tables S5 and S6 in the Supporting Information for peak assignments.

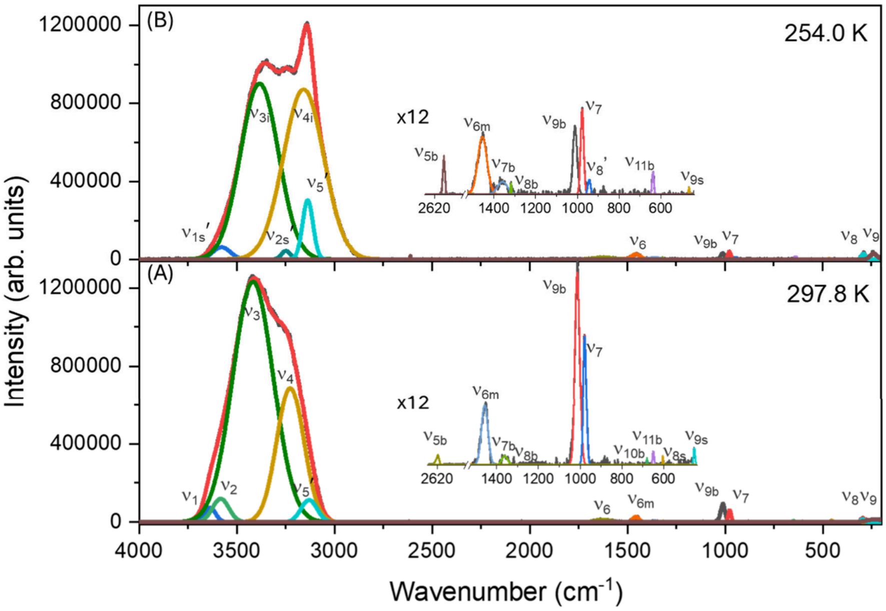

Figure 5. Deconvoluted Raman spectra of a binary 3.5 wt % aqueous solution containing $MgSO_4$ and $NaHCO_3$ in a 1:1 mass ratio, measured at (A) 297.8 K (liquid) and (B) 254.0 K (frozen and equilibrated with the surrounding environment). The 1100–800 cm^{-1} range, capturing overlapping vibrational features of sulfate and bicarbonate species, is magnified to highlight structural and spectral changes upon freezing. Peak details are listed in Tables S7 and S8.

bicarbonate ions. These control experiments were designed to isolate the contributions of each ionic species and to assess their individual spectral signatures under both ambient and frozen conditions.

3.3.1. Freezing of 3.5% w/w Sulfate Solution. In the room temperature spectrum of the pure magnesium sulfate solution (Figure 3), the dominant Raman feature at 981 cm^{-1} is consistent with the symmetric stretching mode of the SO_4^{2-} ion.[48] Detailed peak assignments can be found in Tables S3 and S4. A smaller, yet distinct, peak is also observed near 1015 cm^{-1}, suggesting low-level formation of bisulfate (HSO_4^-) even in the absence of added bicarbonate.[49,73] This may be attributed to mild acidification from Mg^{2+} ions (in the form of $MgSO_4$), which are known to hydrolyze in water and act as weak Lewis acids. Mg^{2+} has a high charge density and strongly polarizes coordinated water molecules, promoting partial deprotonation to form H_3O^+ and lowering the pH of solution.[74] Formation of bisulfate may also be from proton donation by water itself, as bisulfate has a pK_a of 1.92, making SO_4^{2-} sufficiently basic to accept a proton under certain

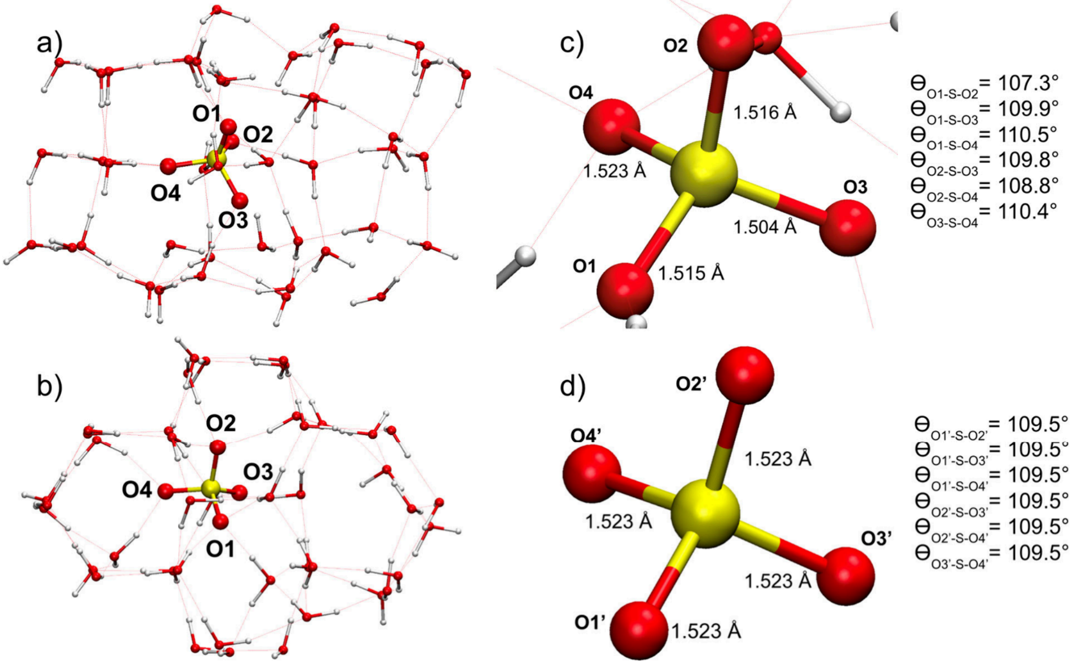

Figure 6. The optimized structure of SO_4^{2-} with 42 water molecules initialized in an ice I_h crystalline structure (a) side view, (b) top view and (c) a close look at the distortion of the sulfate anion exhibited in tetrahedral geometry. (d) SMD water solvated sulfate optimization exhibited in the tetrahedral geometry, where prime atomic labeling indicates a single-molecule optimization.

conditions.[75,76] Another plausible explanation is that the sulfate ion receives a proton from hydronium (H_3O^+), particularly since low-salinity solutions such as ASW or the sulfate solution used here can reach a pH of 6.5 at 258 K or lower.[77] In this case, there cannot be any contribution of phase III Na_2SO_4 to the 1015 cm^{-1} peak as sodium is absent from the solution. Additionally, several secondary sulfate peaks that were previously undetectable in the ASW spectra due to lower sulfate concentration are resolved here. Notably, the ν_{8s} peak, corresponding to the ν_4 bending mode, and the ν_{9s} peak, corresponding to the ν_2 bending mode, are clearly observed and consistent with prior assignments (Table S3).[72]

In the Raman spectrum of the sulfate-only ice crystal, the overall pattern closely mirrors that of frozen ASW: the 981 cm^{-1} peak broadens, and shoulders emerge at approximately 940 and 1015 cm^{-1}. However, in contrast to the room temperature case, the 1015 cm^{-1} peak exhibits markedly reduced intensity under frozen conditions (Table S4). This observation supports the hypothesis that symmetry-lowering effects dominate over bisulfate formation during the freezing process.

3.3.2. Freezing of 3.5% w/w Bicarbonate Solution.

Raman spectrum of the droplet containing bicarbonate solution displays a strong Raman feature near 1015 cm^{-1}, which is characteristic vibration of the C−OH stretching mode of the HCO_3^- ion (Figure 4).[78−80] The increased bicarbonate concentration in this sample, relative to ASW, enables the identification of several additional spectral features. These include the ν_{5b} band at 2620 cm^{-1}, corresponding to the CO−H stretch, and the ν_{7b} and ν_{8b} bands at 1370 and 1309 cm^{-1}, assigned to $-CO_2$ symmetric stretching and C−OH bending, respectively (Table S5).[78,79,81] Two lower-frequency bands are also detected: the ν_{10b} peak at 676 cm^{-1}, associated with CO_2 bending, and the ν_{11b} feature at 642 cm^{-1}, attributed to OCO or HOC deformation modes.[79,81]

Upon freezing, the 1015 cm^{-1} band remains the most intense feature in the bicarbonate spectrum, indicating that freezing induces minimal changes in bicarbonate speciation or coordination. This stands in contrast to the sulfate- and ASW-containing systems, where the freezing process results in considerable spectral broadening and the emergence of new features, further reinforcing the role of sulfate-specific structural transformations.

3.3.3. Freezing of 1:1 Sulfate−Bicarbonate Mixed Solution.

In the room temperature Raman spectrum of the droplet containing 1:1 sulfate-bicarbonate mixture (Figure 5), a strong peak is observed at 1015 cm^{-1}, which exceeds the intensity of the sulfate ν_1 band at 981 cm^{-1}. This dominant feature is primarily attributed to the C−OH stretching vibration of the bicarbonate ion (HCO_3^-).[78−80] In addition to this, nearly all Raman-active modes identified in the individual sulfate and bicarbonate solutions are also present in this mixed system (Table S7). On the high-wavenumber end, the ν_{5b} band at 2620 cm^{-1} corresponding to the CO−H stretch of bicarbonate is detected. The spectrum also includes ν_{7b}, ν_{8b}, ν_{9b}, ν_{10b}, and ν_{11b} bands, all previously observed in the pure bicarbonate solution, as well as the sulfate-associated ν_7, ν_{8s}, and ν_{9s} bands found in the pure sulfate solution.

Upon freezing, the 1015 cm^{-1} peak persists but decreases in intensity relative to the 981 cm^{-1} sulfate band, and the characteristic ν_7'/ ν_8' sulfate shoulder features observed in ASW and pure sulfate solutions are not distinctly resolved in the mixed system, indicating that bicarbonate has little influence on the coordination or symmetry of the sulfate anion under frozen conditions (Table S8). Notably, the appearance of a band at 1458 cm^{-1} (ν_{6m}) assigned to the C−O stretching mode of the carbonate ion (CO_3^{2-}) in both room temperature and frozen spectra of the 1:1 mixture provides further evidence for partial carbonate formation.[81−83] This feature is absent in all other samples, indicating that comparable concentrations of sulfate and bicarbonate (pK_a

10.33) may favor this deprotonation transformation pathway.[76] On the other hand, plausible formation of bisulfate can be masked under the dominant features of bicarbonate.

Some Raman bands evident at room temperature such as the ν_{10b} mode of bicarbonate and the ν_{8s} sulfate bending mode are no longer observed in the spectrum of the ice crystal. This trend is consistent with a broader pattern of intensity loss upon freezing, which may be attributed to increased structural disorder or symmetry changes in the frozen matrix, similar to the effects observed for the sulfate ν_7 band. In addition, it is noteworthy here that in the high-wavenumber OH-stretch region, all four droplets studied saw a redshift in the dominant bands ν_3 and ν_4 and are given new assignments ν_{3i} and ν_{4i}, respectively, to reflect this decrease in wavenumbers. This is expected considering the increase in oscillatory strength of hydrogen-bonds upon freezing.[61] A comparison of the OH-stretch region of the four droplets and their crystals can be found in Figures S5 and S6, and Tables S9−S16 depict the list of detailed peak locations and fwhm's of the bands of the deconvoluted regions.

3.4. Computational Analysis. The vibrational frequencies of the SO_4^{2-}, CO_3^{2-}, and HCO_3^- anions in the ice are computed according to Section 2.4. Geometry optimizations show that the incorporation of SO_4^{2-} into the hexagonal-ice hydrogen-bonded network produces inequivalent S−O bond lengths (150−152 nm) and deviations from ideal O−S−O angles (±1.2°) lowering the local symmetry from the tetrahedral point group (T_d) to C_1 (Figure 6). The normal-mode analysis (Table 3) indicates that the totally symmetric S−O stretch is extensively coupled with surrounding water molecules and thus becomes active across several nearby modes in hexagonal-ice rather than appearing at a single frequency. As the neighboring molecules do not hold tetrahedral symmetry around SO_4^{2-}, the coupling results in the observed inhomogeneous broadening with partially resolved shoulders of the symmetric stretch Raman band upon freezing.

Table 3. Frequency Calculation Results for Sulfate in Solution and in the Ice Crystal

Vibrational mode	SMD water solvated model wavenumber (cm^{-1})	Ice-encapsulated model active wavenumbers (cm^{-1})
Sulfate symmetric stretch	856	886
		892
		895
		908
Carbonate symmetric stretch	978	1057
		1053
		1031
		1028

The most rigorous study of the vibrational frequencies of SO_4^{2-} in liquid water should sample a large configurational space with *ab initio* molecule dynamics (AIMD) simulations to account for different arrangements of the hydrogen-bond network, so that local distortions can be averaged over all these configurations.[84] Since extensive AIMD simulations are well beyond the scope of this work, we employed a continuum model, SMD to account for the liquid phase. It is worth noting that the absolute frequencies these calculations should not be directly compared with the experiment due to the finite size cluster (for ice) and implicit solvent (for liquid); the focus should be on the structural distortions and spectral broadening.[85]

Figures 7 and 8 show the geometry optimization of CO_3^{2-} and HCO_3^- in the condensed phase. Similar to the case of SO_4^{2-}, the encapsulated environment of hexagonal ice introduces a fair amount of geometry distortion to both CO_3^{2-} and HCO_3^-. Since the symmetric sulfate stretch involves concerted motion from all four S−O bonds, it is intrinsically sensitive to symmetry breaking. In contrast, since HCO_3^- is of lower symmetry (C_s) and the C−OH stretch is highly localized, general distortions of the asymmetric interactions from neighboring water molecules couple only indirectly to the Raman band. Although CO_3^{2-} is of high symmetry (D_{3h}) and the calculations predict similar freezing-induced broadening of the symmetric C−O stretch as observed in the symmetric S−O stretch (Table 3), the experimental carbonate abundance in the droplet is too low to validate the prediction.

4. CONCLUSION

Using Raman spectroscopy on levitated droplets of artificial seawater (ASW) and model salt solutions in a simulated atmosphere, this study examined ion speciation and structural changes during freezing under conditions that closely resemble atmospheric aerosols. The droplet levitation method eliminates container wall effects and, with the high surface-to-volume ratio for the microliter-sized droplets, enables the study of the enhanced interfacial chemistry compared to bulk-phase systems.

Droplet freezing of ASW and the pure sulfate control solution resulted in a broadening of the sulfate ν_1 band at 981 cm^{-1} and production of additional peaks near 940 and ∼1014 cm^{-1}, consistent with reduced-symmetry sulfate environments and possible bisulfate formation. Collectively, our results support three key conclusions: (1) the broadening of the sulfate peak upon freezing is primarily driven by symmetry reduction and heterogeneity in local solvation environments; (2) control experiments show that while bicarbonate serves as a useful control for distinguishing overlapping vibrational features, sulfate emerges as the pivotal component that initiates distinct ionic conversion during ice formation in seawater, while possibly also enhancing reactive interfacial interactions due to increased acidity; and (3) ASW contains insufficient bicarbonate to promote any significant bisulfate formation or self-conversion to carbonate, thus exhibiting only very weak features beyond the dominant sulfate band. Although the present measurements probe the bulk composition of the droplets, the Raman signatures alone cannot determine whether the potential bisulfate formation occurs primarily in the bulk phase, at the air−liquid interface, or in both regions. Future studies employing interface-specific techniques, such as (liquid jet) photoelectron spectroscopy, would therefore be highly valuable for resolving the interfacial contributions and providing a more complete picture of the freezing-induced ionic transformations in these systems.

In addition, these results have direct implications for the atmospheric chemistry of frozen aerosols, including the uptake and transformation of acidic gases such as sulfur dioxide (SO_2), hydrogen chloride (HCl), hydrofluoric acid (HF), and common fluorinated refrigerant gases (hydrofluorocarbons

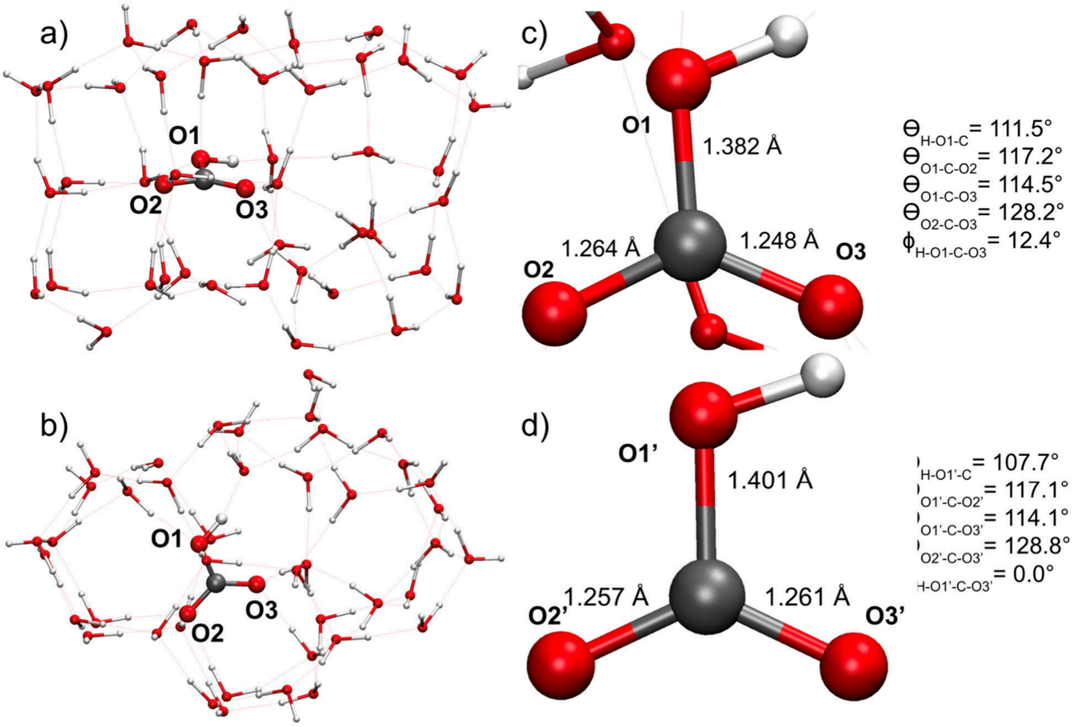

Figure 7. The optimized structure of HCO_3^- with 42 water molecules initialized in an ice I_h crystalline structure (a) side view, (b) top view and (c) a close look at the distortion of the bicarbonate anion from the C_s symmetry. (d) SMD water solvated bicarbonate optimization exhibited in C_s, where prime atomic labeling indicates a single-molecule optimization.

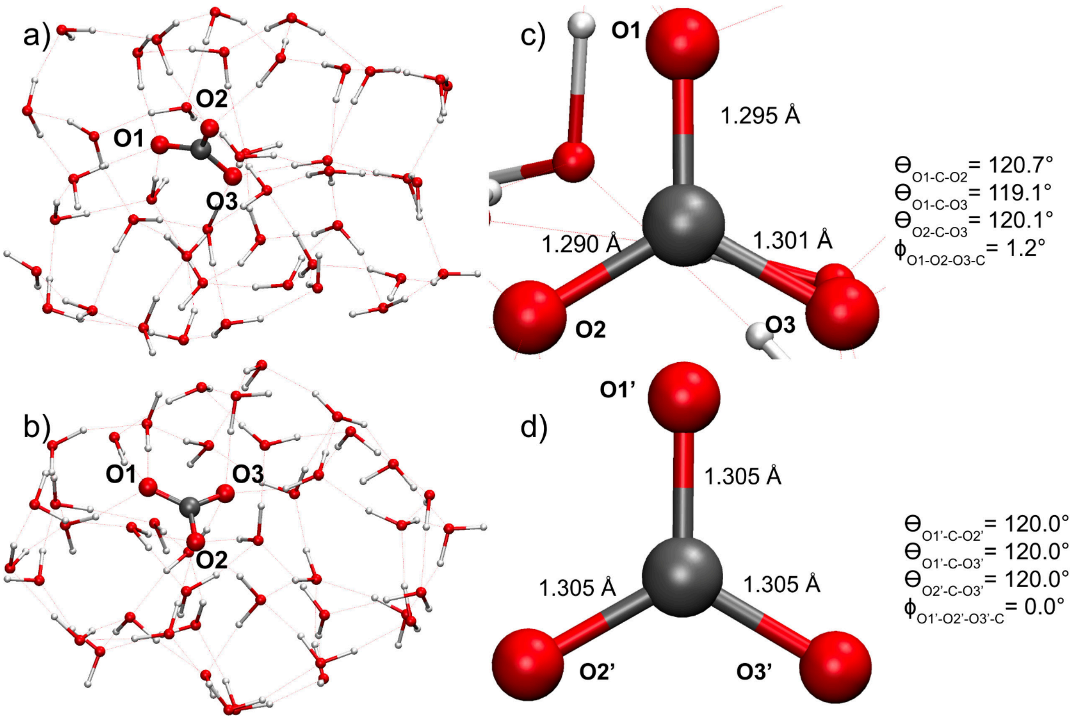

Figure 8. The optimized structure of CO_3^{2-} with 42 water molecules initialized in an ice I_h crystalline structure (a) side view, (b) top view and (c) a close look at the distortion of the carbonate anion from the D_{3h} symmetry. (d) SMD water solvated carbonate optimization exihibited in D_{3h} geometry, where prime atomic labeling indicates a single-molecule optimization.

(HFCs), hydrofluoroolefins (HFOs), hydrochlorofluorocarbons (HCFCs)) with their degradation products such as trifluoracetic acid (TFA). Sulfate uptake has been shown to initiate diverse atmospheric reactions. For example, nitrate photolysis in the presence of SO_2 can generate nitric oxide (NO_2), thereby enhancing sulfate production under high-nitrate conditions. Similarly, heterogeneous uptake of SO_2 onto urban surfaces has been linked to the formation of organic sulfur compounds and haze episodes.[86,87] These cases illustrate how sulfate-driven droplet and interfacial chemistry can redirect multiphase pathways and amplify secondary pollutant formation. In this context, the interactions of sulfate with emerging atmospheric constituents such as halogenated refrigerants are especially relevant to decipher their long-range transport and degradation mechanism. Salt phase segregation in ice, such as hydrohalite and antarcticite formation, may strongly bind halides and alter pollutant reactivity and lifetime.[88] By combining chemical specificity with a geometry that mimics atmospheric particles, this approach provides a framework for predicting reactivity, phase behavior, and pollutant uptake in frozen marine and mixed aerosols under cold environmental conditions.

■ ASSOCIATED CONTENT

Supporting Information

The Supporting Information is available free of charge at https://pubs.acs.org/doi/10.1021/acs.jpca.5c06239.

> Photograph of the levitator setup, Raman spectra and peak assignments of pure water, visualization and temporal profiles of the freezing event, peak assignments of deconvoluted spectra, deconvoluted OH-stretch region of all four droplets and peak widths (PDF)

■ AUTHOR INFORMATION

Corresponding Author

Ralf Kaiser − Department of Chemistry, University of Hawai'i at Manoa, Honolulu, Hawaii 96822, United States; orcid.org/0000-0002-7233-7206; Email: ralfk@hawaii.edu

Authors

Frank Liang − Department of Chemistry, University of Hawai'i at Manoa, Honolulu, Hawaii 96822, United States
Souvick Biswas − Department of Chemistry, University of Hawai'i at Manoa, Honolulu, Hawaii 96822, United States; orcid.org/0000-0002-1643-2663
Nils W. Melbourne − Department of Chemistry, University of Hawai'i at Manoa, Honolulu, Hawaii 96822, United States; orcid.org/0000-0003-0495-6790
Koushik Mondal − Department of Chemistry, University of Hawai'i at Manoa, Honolulu, Hawaii 96822, United States
Rui Sun − Department of Chemistry, University of Hawai'i at Manoa, Honolulu, Hawaii 96822, United States; orcid.org/0000-0003-0638-1353

Complete contact information is available at: https://pubs.acs.org/10.1021/acs.jpca.5c06239

Notes

The authors declare no competing financial interest.

■ ACKNOWLEDGMENTS

This study was funded through the NSF award, 2330175, Center: NSF Engineering Research Center for Environmentally Applied Refrigerant Technology Hub. The authors appreciate the Information Technology Service (ITS) from the University of Hawaii at Manoa for the computational resources.

■ REFERENCES

(1) How Much Water is There on Earth?, U.S. Geological Survey. https://www.usgs.gov/water-science-school/science/how-much-water-there-earth (accessed 2025-08-11).

(2) Libes, S. *Introduction to marine biogeochemistry*; Academic Press: 2011.

(3) Lyman, J.; Fleming, R. H. Composition of sea water. *J. Mar. Res.* **1940**, 1.

(4) Lebrato, M.; Garbe-Schönberg, D.; Müller, M. N.; Blanco-Ameijeiras, S.; Feely, R. A.; Lorenzoni, L.; Molinero, J.-C.; Bremer, K.; Jones, D. O.; Iglesias-Rodriguez, D. Global variability in seawater Mg: Ca and Sr: Ca ratios in the modern ocean. *Proc. Natl. Acad. Sci. U. S. A* **2020**, *117* (36), 22281−22292.

(5) Carpenter, K.; Bahadur, V. Saltwater icephobicity: Influence of surface chemistry on saltwater icing. *Sci. Rep.* **2015**, *5* (1), 17563.

(6) Olson, S.; Jansen, M. F.; Abbot, D. S.; Halevy, I.; Goldblatt, C. The effect of ocean salinity on climate and its implications for Earth's habitability. *Geophys. Res. Lett.* **2022**, *49* (10), No. e2021GL095748.

(7) Collins, K. D. Charge density-dependent strength of hydration and biological structure. *Biophys. J.* **1997**, *72* (1), 65−76.

(8) Hribar, B.; Southall, N. T.; Vlachy, V.; Dill, K. A. How ions affect the structure of water. *J. Am. Chem. Soc.* **2002**, *124* (41), 12302−12311.

(9) Zhang, S.; Zhang, C.; Wu, S.; Zhou, X.; He, Z.; Wang, J. Ion-specific effects on the growth of single ice crystals. *J. Phys. Chem. Lett.* **2021**, *12* (36), 8726−8731.

(10) Schwidetzky, R.; Lukas, M.; YazdanYar, A.; Kunert, A. T.; Pöschl, U.; Domke, K. F.; Fröhlich-Nowoisky, J.; Bonn, M.; Koop, T.; Nagata, Y. Specific ion−protein interactions influence bacterial ice nucleation. *Chem. - A Eur. J.* **2021**, *27* (26), 7402−7407.

(11) Chu, F.; Li, S.; Zhao, C.; Feng, Y.; Lin, Y.; Wu, X.; Yan, X.; Miljkovic, N. Interfacial ice sprouting during salty water droplet freezing. *Nat. Commun.* **2024**, *15* (1), 2249.

(12) Ye, Y.; Shokr, M.; Zhuo-Qi, C.; Cheng, X. Exploring the effect of Arctic perennial sea ice on modulation of local air temperature. *Adv. Clim. Chang. Res.* **2022**, *13* (4), 473−488.

(13) Cornish, S.; Johnson, H.; Mallett, R.; Dörr, J.; Kostov, Y.; Richards, A. Rise and fall of sea ice production in the Arctic Ocean's ice factories. *Nat. Commun.* **2022**, *13* (1), 7800.

(14) Jørgensen, B. B.; Findlay, A. J.; Pellerin, A. The biogeochemical sulfur cycle of marine sediments. *Front. Microbiol.* **2019**, *10*, 849.

(15) Wasmund, K.; Mußmann, M.; Loy, A. The life sulfuric: microbial ecology of sulfur cycling in marine sediments. *Envir. microb. rep.* **2017**, *9* (4), 323−344.

(16) Middelburg, J. J.; Soetaert, K.; Hagens, M. Ocean alkalinity, buffering and biogeochemical processes. *Rev. Geophys.* **2020**, *58* (3), No. e2019RG000681.

(17) Poschenrieder, C.; Fernández, J. A.; Rubio, L.; Pérez, L.; Terés, J.; Barceló, J. Transport and use of bicarbonate in plants: current knowledge and challenges ahead. *Int. J. Mol. Sci.* **2018**, *19* (5), 1352.

(18) Ackerman, K. L.; Nugent, A. D.; Taing, C. Mechanisms controlling giant sea salt aerosol size distributions along a tropical orographic coastline. *Atmos. Chem. Phys.* **2023**, *23* (21), 13735−13753.

(19) Lawler, M. J.; Schill, G. P.; Brock, C. A.; Froyd, K. D.; Williamson, C.; Kupc, A.; Murphy, D. M. Sea spray Aerosol over the remote Oceans has low Organic content. *AGU Adv.* **2024**, *5* (4), No. e2024AV001215.

(20) Alpert, P. A.; Kilthau, W. P.; O'Brien, R. E.; Moffet, R. C.; Gilles, M. K.; Wang, B.; Laskin, A.; Aller, J. Y.; Knopf, D. A. Ice-nucleating agents in sea spray aerosol identified and quantified with a holistic multimodal freezing model. *Sci. Adv.* **2022**, *8* (44), No. eabq6842.

(21) Knopf, D.; Barry, K.; Brubaker, T.; Jahl, L.; Jankowski, K.; Li, J.; Lu, Y.; Monroe, L.; Moore, K.; Rivera-Adorno, F. Aerosol−ice formation closure: A Southern Great Plains field campaign. *Bull. Am. Meteorol. Soc.* **2021**, *102* (10), E1952−E1971.

(22) Lin, Y.; Fan, J.; Li, P.; Leung, L. R.; DeMott, P.; Goldberger, L.; Comstock, J.; Liu, Y.; Jeong, J.; Tomlinson, J. Impacts of ice-nucleating particles from marine aerosols on mixed-phase orographic clouds during 2015 ACAPEX field campaign. *Atmos. Chem. Phys.* **2021**, *2021*, 1−49.

(23) Mitts, B. A.; Wang, X.; Lucero, D. D.; Beall, C. M.; Deane, G. B.; DeMott, P. J.; Prather, K. A. Importance of supermicron ice nucleating particles in nascent sea spray. *Geophys. Res. Lett.* **2021**, *48* (3), No. e2020GL089633.

(24) Wolf, M. J.; Goodell, M.; Dong, E.; Dove, L. A.; Zhang, C.; Franco, L. J.; Shen, C.; Rutkowski, E. G.; Narducci, D. N.; Mullen, S. A link between the ice nucleation activity and the biogeochemistry of seawater. *Atmos. Chem. Phys.* **2020**, *20* (23), 15341−15356.

(25) Thornton, D. C.; Brooks, S. D.; Wilbourn, E. K.; Mirrielees, J.; Alsante, A. N.; Gold-Bouchot, G.; Whitesell, A.; McFadden, K. Production of ice-nucleating particles (INPs) by fast-growing phytoplankton. *Atmos. Chem. Phys.* **2023**, *23* (19), 12707−12729.

(26) Yang, Y.; Wang, H.; Huang, W.; Gao, Y.; Li, Z.; Wang, X. Ion migration during freeze-thaw process: a cryo-desalination experiment of saltwater from southern Xinjiang, China. *Desalination* **2022**, *544*, No. 116118.

(27) Zhao, H.; Wu, J.; Peng, Z.; Wu, Z. Ion migration at the ice−water interface during the freezing process of salt solution−experimental investigation. *Desalination* **2024**, *592*, No. 118172.

(28) Zhao, H.; Wu, J.; Peng, Z.; Wu, Z. Ion migration at the ice−water interface during the freezing process of salt solution−Numerical investigation. *Int. J. Therm. Sci.* **2025**, *215*, No. 110017.

(29) Gholami, S.; Buttersack, T.; Richter, C.; Trinter, F.; Dupuy, R.; Cablitz, L.; Zhou, Q.; Nicolas, C.; Shavorskiy, A.; Diaman, D. Interaction of ions and surfactants at the seawater−air interface. *Environmental Science: Atmospheres* **2025**, *5* (3), 291−299.

(30) Bauerecker, S.; Buttersack, T. Electric effect during the fast dendritic freezing of supercooled water droplets. *J. Phys. Chem. B* **2014**, *118* (47), 13629−13635.

(31) Bullister, J.; Weiss, R. Anthropogenic chlorofluoromethanes in the Greenland and Norwegian Seas. *Sci.* **1983**, *221* (4607), 265−268.

(32) Ito, T.; Marshall, J.; Follows, M. What controls the uptake of transient tracers in the Southern Ocean? *Global Biogeochem. Cycles* **2004**, *18* (2), 1.

(33) Romanou, A.; Marshall, J.; Kelley, M.; Scott, J. Role of the ocean's AMOC in setting the uptake efficiency of transient tracers. *Geophys. Res. Lett.* **2017**, *44* (11), 5590−5598.

(34) Waugh, D. W. Changes in the ventilation of the southern oceans. *Philos. Trans. R. Soc. A Math. Phys. Eng. Sci.* **2014**, *372* (2019), No. 20130269.

(35) Wang, P.; Solomon, S.; Lickley, M.; Scott, J. R.; Weiss, R. F.; Prinn, R. G. On the influence of hydroxyl radical changes and ocean sinks on estimated HCFC and HFC emissions and banks. *Geophys. Res. Lett.* **2023**, *50* (18), No. e2023GL105472.

(36) Biswas, S.; Paul, D.; Mondal, K.; Kaiser, R. I. Simulating atmospheric freezing of single aqueous droplets to ice in a cryogenically cooled ultrasonic levitator. *Proc. Natl. Acad. Sci. U. S. A.* **2025**, *122* (6), No. e2425543122.

(37) Mondal, K.; Biswas, S.; Melbourne, N.; Sun, R.; Kaiser, R. I. Probing the freezing chemistry of singly levitated aqueous trifluoroacetic acid droplets in a cryogenically cooled simulation chamber relevant to Earth's upper troposphere. *Chem. Sci.* **2025**, *16*, 11039−11048.

(38) Bauerecker, S.; Ulbig, P.; Buch, V.; Vrbka, L.; Jungwirth, P. Monitoring ice nucleation in pure and salty water via high-speed imaging and computer simulations. *J. Phys. Chem. C* **2008**, *112* (20), 7631−7636.

(39) Foltz, K. R.; Adams, N. L.; Runft, L. L. Echinoderm eggs and embryos: procurement and culture. *Methods Cell Biol.* **2004**, *74*, 39−74.

(40) Rizzo, G. L.; Biswas, S.; Antonov, I.; Miller, K. K.; Pantoya, M. L.; Kaiser, R. I. Exotic Inverse Kinetic Isotopic Effect in the Thermal Decomposition of Levitated Aluminum Iodate Hexahydrate Particles. *J. Phys. Chem. Lett.* **2023**, *14* (11), 2722−2730.

(41) Biswas, S.; Mcanally, M.; Chambreau, S. D.; Schneider, S.; Sun, R.; Kaiser, R. I. Atmospheric Ignition Chemistry of Green Hypergolic Bipropellant 1-Ethyl-3-Methylimidazolium Cyanoborohydride−Hydrogen Peroxide in an Acoustic Levitator: Exploring a Potent Universal Propellant. *Chem. − A Eur. J.* **2025**, *31* (23), No. e202500593.

(42) Marenich, A. V.; Cramer, C. J.; Truhlar, D. G. Universal solvation model based on solute electron density and on a continuum model of the solvent defined by the bulk dielectric constant and atomic surface tensions. *j. phys. Chem. B* **2009**, *113* (18), 6378−6396.

(43) Apra, E.; Bylaska, E. J.; De Jong, W. A.; Govind, N.; Kowalski, K.; Straatsma, T. P.; Valiev, M.; van Dam, H. J.; Alexeev, Y.; Anchell, J. NWChem: Past, present, and future. *J. Chem. Phys.* **2020**, *152* (18), 18410.

(44) DiLabio, G. A.; Johnson, E. R.; Otero-de-la-Roza, A. Performance of conventional and dispersion-corrected density-functional theory methods for hydrogen bonding interaction energies. *Phys. Chem. Chem. Phys.* **2013**, *15* (31), 12821−12828.

(45) Computational Chemistry Comparison and Benchmark DataBase Release 22 (May 2022) Standard Reference Database 101 National Institute of Standards and Technology, available online: https://cccbdb.nist.gov/vibscalejustx.asp.

(46) Hanwell, M. D.; Curtis, D. E.; Lonie, D. C.; Vandermeersch, T.; Zurek, E.; Hutchison, G. R. Avogadro: an advanced semantic chemical editor, visualization, and analysis platform. *J. cheminfo.* **2012**, *4* (1), 17.

(47) Humphrey, W.; Dalke, A.; Schulten, K. VMD: visual molecular dynamics. *J. mol. graph.* **1996**, *14* (1), 33−38.

(48) Ben Mabrouk, K.; Kauffmann, T. H.; Aroui, H.; Fontana, M. D. Raman study of cation effect on sulfate vibration modes in solid state and in aqueous solutions. *J. Raman Spectrosc.* **2013**, *44* (11), 1603−1608.

(49) Xi, S.; Zhang, X.; Luan, Z.; Du, Z.; Li, L.; Wang, B.; Cao, L.; Lian, C.; Yan, J. A direct quantitative Raman method for the measurement of dissolved bisulfate in acid-Sulfate fluids. *Appl. Spectrosc.* **2018**, *72* (8), 1234−1243.

(50) Sun, Q.; Zheng, H. Raman OH stretching vibration of ice I_h. *Prog. Nat. Sci.* **2009**, *19* (11), 1651−1654.

(51) Wernet, P.; Nordlund, D.; Bergmann, U.; Cavalleri, M.; Odelius, M.; Ogasawara, H.; Naslund, L. A.; Hirsch, T.; Ojamae, L.; Glatzel, P. The structure of the first coordination shell in liquid water. *Science* **2004**, *304* (5673), 995−999.

(52) Smit, W. J.; Tang, F.; Nagata, Y.; Sánchez, M. A.; Hasegawa, T.; Backus, E. H.; Bonn, M.; Bakker, H. J. Observation and identification of a new OH stretch vibrational band at the surface of ice. *J. Phys. Chem. Lett.* **2017**, *8* (15), 3656−3660.

(53) Dong, C.; Liu, Y.; Han, T.; Zhou, X.; Meng, Y.; Tian, Y.; Ma, L. Effect of hydrated ions and wettability on ice friction. *Friction* **2025**, *13* (7), 9440972.

(54) Walrafen, G. E. Raman and infrared spectral investigations of water structure. *The Physics and Physical Chemistry of Water*; Springer: 1972; pp 151−214.

(55) Smith, J. D.; Cappa, C. D.; Drisdell, W. S.; Cohen, R. C.; Saykally, R. J. Raman thermometry measurements of free evaporation from liquid water droplets. *J. Am. Chem. Soc.* **2006**, *128* (39), 12892−12898.

(56) Goy, C.; Potenza, M. A.; Dedera, S.; Tomut, M.; Guillerm, E.; Kalinin, A.; Voss, K.-O.; Schottelius, A.; Petridis, N.; Prosvetov, A. Shrinking of rapidly evaporating water microdroplets reveals their extreme supercooling. *Phys. Rev. Lett.* **2018**, *120* (1), No. 015501.

(57) Furić, K.; Volovšek, V. Water ice at low temperatures and pressures: New Raman results. *J. Mol. Struct.* **2010**, *976* (1−3), 174−180.

(58) Walrafen, G. Raman spectral studies of the effects of temperature on water structure. *J. Chem. Phys.* **1967**, *47* (1), 114−126.

(59) Risović, D.; Furić, K. Comparison of Raman spectroscopic methods for the determination of supercooled and liquid water temperature. *Journal of Raman Spectroscopy: An International Journal for Original Work in all Aspects of Raman Spectroscopy, Including Higher Order Processes, and also Brillouin and Rayleigh Scattering* **2005**, *36* (8), 771−776.

(60) Dubessy, J.; Audeoud, D.; Wilkins, R.; Kosztolanyi, C. The use of the Raman microprobe MOLE in the determination of the electrolytes dissolved in the aqueous phase of fluid inclusions. *Chem. Geol.* **1982**, *37* (1−2), 137−150.

(61) Liu, Y.; Ojamae, L. Raman and IR spectra of ice Ih and ice XI with an assessment of DFT methods. *J. Phys. Chem. B* **2016**, *120* (42), 11043−11051.

(62) Tuschel, D. Stress, strain, and Raman spectroscopy. *Spectroscopy* **2019**, *34* (9).

(63) Periasamy, A.; Muruganand, S.; Palaniswamy, M. Vibrational studies of Na_2SO4, K_2SO_4, $NaHSO_4$ and $KHSO_4$ crystals. *Rasayan J. Chem.* **2009**, *2* (4), 981−989.

(64) Garcia, C. S.; Abedin, M. N.; Sharma, S. K.; Misra, A. K.; Ismail, S.; Singh, U. N.; Refaat, T. F.; Elsayed-Ali, H. E.; Sandford, S. P. Remote pulsed laser Raman spectroscopy system for detecting water, ice, and hydrous minerals; Imaging Spectrometry XI; SPIE: 2006; pp 296−302.

(65) Fukazawa, H.; Mae, S.; Ikeda, S. Raman scattering and neutron-diffraction studies of fresh ice and Antarctic ice. *Ann. Glaciol.* **2000**, *31*, 247−251.

(66) Wang, Z.; Pakoulev, A.; Pang, Y.; Dlott, D. D. Vibrational substructure in the OH stretching transition of water and HOD. *J. Phys. Chem. A* **2004**, *108* (42), 9054−9063.

(67) Baumgartner, M.; Bakker, R. J. Raman spectroscopy of pure H_2O and NaCl-H_2O containing synthetic fluid inclusions in quartz—a study of polarization effects. *Mineralogy and Petrology* **2009**, *95* (1), 1−15.

(68) Shigenari, T.; Abe, K. Vibrational modes of hydrogens in the proton ordered phase XI of ice: Raman spectra above 400 cm^{-1}. *J. Chem. Phys.* **2012**, *136* (17), 174504.

(69) Wong, P.; Whalley, E. Optical spectra of orientationally disordered crystal. V. Raman spectrum of ice I_h in the range 4000−350 cm^{-1}. *J. Chem. Phys.* **1975**, *62* (6), 2418−2425.

(70) Bergren, M. S.; Schuh, D.; Sceats, M. G.; Rice, S. A. The OH stretching region infrared spectra of low density amorphous solid water and polycrystalline ice Ih. *J. Chem. Phys.* **1978**, *69* (8), 3477−3482.

(71) Tran, L. K.; Stepien, K. R.; Bollmeyer, M. M.; Yoder, C. H. Substitution of sulfate in apatite. *Am. Mineral.* **2017**, *102* (10), 1971−1976.

(72) Frost, R. L.; Xi, Y.; Scholz, R.; López, A.; Granja, A. Infrared and Raman spectroscopic characterisation of the sulphate mineral creedite−$Ca_3Al_2SO_4$ (F, OH)· $2H_2O$−and in comparison with the alums. *Spectrochim. Acta - Part A Mol. Biomol. Spectrosc.* **2013**, *109*, 201−205.

(73) Cooke, M. E.; Alotbi, A. R.; Waters, C. M.; Heagle, L. J.; Armstrong, N. C.; Poworoznek, C. J.; Zhang, Z.; Gold, A.; Surratt, J. D.; Ault, A. P. Acidity-Driven Shifts in Aerosolized Sodium Sulfate Crystal Structure via Raman Microspectroscopy and Implications for Isoprene-Derived Secondary Organic Aerosol Formation. *J. Phys. Chem. A* **2025**, *129*, 7451−7460.

(74) Jurinak, J. J. The Hydrolysis of Cations. *Soil Sci. Soc. Am. J.* **1976**, *40* (3), vi.

(75) Timberlake, K. *Chemistry: an introduction to general, organic, and biological chemistry*; 2009.

(76) Bruice, P. Y. *Organic Chemistry, Global Edition*; Pearson Education Limited: 2016.

(77) Veselý, L.; Štůsek, R.; Mikula, O.; Yang, X.; Heger, D. Freezing-induced acidification of sea ice brine. *Sci. Total Environ.* **2024**, *946*, No. 174194.

(78) Falcke, H.; Eberle, S. Raman spectroscopic identification of carbonic acid. *Water Res.* **1990**, *24* (6), 685−688.

(79) Rudolph, W. W.; Irmer, G.; Königsberger, E. Speciation studies in aqueous HCO_3^-−CO_3^{2-} solutions. A combined Raman spectroscopic and thermodynamic study. *J. Chem. Soc. Dalt. Trans.* **2008**, No. 7, 900−908.

(80) Swartzwelder, A. D. *Raman spectroscopy of the CO_2-H_2O system*; The Ohio State University: 2006.

(81) Frantz, J. D. Raman spectra of potassium carbonate and bicarbonate aqueous fluids at elevated temperatures and pressures: comparison with theoretical simulations. *Chem. Geol.* **1998**, *152* (3−4), 211−225.

(82) Alves, J. F.; Edwards, H. G.; Korsakov, A.; De Oliveira, L. F. C. Revisiting the Raman spectra of carbonate minerals. *Minerals* **2023**, *13* (11), 1358.

(83) Bissengaliyeva, M. Calculations of the structural and thermodynamic characteristics of copper carbonates by quantum-chemical methods. *Russ. J. Phys. Chem. A* **2009**, *83* (2), 238−244.

(84) Thomas, M. *Theoretical modeling of vibrational spectra in the liquid phase*; Springer: 2016.

(85) Giovannini, T.; Cappelli, C. Continuum vs. atomistic approaches to computational spectroscopy of solvated systems. *Chem. Com.* **2023**, *59* (38), 5644−5660.

(86) Deng, H.; Lakey, P. S.; Wang, Y.; Li, P.; Xu, J.; Pang, H.; Liu, J.; Xu, X.; Li, X.; Wang, X. Daytime SO2 chemistry on ubiquitous urban surfaces as a source of organic sulfur compounds in ambient air. *Sci. Adv.* **2022**, *8* (39), No. eabq6830.

(87) Cai, S.; Liu, T.; Huang, X.; Song, Y.; Wang, T.; Sun, Z.; Gao, J.; Ding, A. Important role of low cloud and fog in sulfate aerosol formation during winter haze over the North China Plain. *Geophys. Res. Lett.* **2024**, *51* (3), No. e2023GL106597.

(88) Light, B.; Brandt, R. E.; Warren, S. G. Hydrohalite in cold sea ice: Laboratory observations of single crystals, surface accumulations, and migration rates under a temperature gradient, with application to "Snowball Earth". *J. Geophys. Res. Ocean* **2009**, *114* (C7), C07018.